




## Magnetic structure of the swedenborgite compound $\text{CaBaMn}_2\text{Fe}_2\text{O}_7$ derived by powder neutron diffraction and Mössbauer spectroscopy

N. Qureshi <sup>1,\*</sup>, R. Morrow <sup>2</sup>, M. Valldor <sup>3</sup>, I. Puente-Orench,<sup>1,4</sup> and P. Adler<sup>5</sup>

<sup>1</sup>*Institut Laue-Langevin, 71 avenue des Martyrs, CS 20156, 38042 Grenoble Cedex 9, France*

<sup>2</sup>*Leibniz Institute for Solid State and Materials Research IFW Dresden, Helmholtzstraße 20, 01069 Dresden, Germany*

<sup>3</sup>*Centre for Materials Science and Nanotechnology (SMN), Department of Chemistry, University of Oslo, 0315 Oslo, Norway*

<sup>4</sup>*Instituto de Nano Ciencia y Materiales de Aragón, CSIC-Universidad de Zaragoza, 50009 Zaragoza, Spain*

<sup>5</sup>*Max-Planck-Institut für Chemische Physik fester Stoffe, 01187 Dresden, Germany*



(Received 28 July 2022; revised 6 October 2022; accepted 7 October 2022; published 24 October 2022)

We present a study combining neutron diffraction and  $^{57}\text{Fe}$  Mössbauer spectroscopy on a powder sample of  $\text{CaBaMn}_2\text{Fe}_2\text{O}_7$  belonging to the large family of swedenborgite compounds. The undistorted hexagonal crystal structure (space group  $P6_3mc$ ) is preserved down to low temperatures, and all employed techniques reveal a transition into a magnetically long-range ordered phase at  $T_N = 205$  K. The magnetic Bragg peak intensities from the powder diffraction patterns together with a symmetry analysis of the employed models unambiguously reveal the classical  $\sqrt{3} \times \sqrt{3}$  magnetic structure on a hexagonal lattice with propagation vector  $\mathbf{q} = (\frac{1}{3} \frac{1}{3} 0)$ . The nuclear Bragg peak intensities allowed the statistical distribution of Fe and Mn ions on both trigonal and kagome sites of the complex swedenborgite structure to be analyzed which was considered to explain the complex shape of the Mössbauer spectra.

DOI: [10.1103/PhysRevB.106.144428](https://doi.org/10.1103/PhysRevB.106.144428)

### I. INTRODUCTION

Crystal structures based on vertex-sharing triangles, e.g., kagome layers [1,2] or pyrochlore nets [3,4], coupled with antiferromagnetic exchange interactions between nearest neighbors lead to the well-known phenomenon of geometrical frustration [5,6], meaning that not all exchange interactions can be satisfied simultaneously. Compounds with a high degree of frustration may remain magnetically disordered down to low temperatures despite strong coupling between the magnetic moments, but often small distortions, resulting in unequal bond lengths, relieve the geometrical frustration and may lead to exotic magnetic structures with equally fascinating properties. Swedenborgites are the structural homologue to the hexagonal mineral  $\text{SbNaBe}_4\text{O}_7$  [7,8] and may feature transition metal (TM) ions forming kagome planes separated by layers with trigonal symmetry which has been reported for  $\text{YBaCo}_4\text{O}_7$  [9]. In this hexagonal compound, only short-range magnetic order was observed based on the diffuse neutron scattering from powder samples, and by diluting the magnetic lattice with a nonmagnetic ion in  $\text{YBa}(\text{Co}_{4-x}\text{Zn}_x)\text{O}_7$  ( $x = 0-3$ ), the properties gradually change into a spin-glass [9,10]. A chiral spin-liquid ground state has been reported for  $\text{YBaCo}_3\text{FeO}_7$  in which antisymmetric magnetic diffuse scattering was observed using single-crystal neutron diffraction with XYZ polarization analysis [11].  $\text{CaBaCo}_2\text{Fe}_2\text{O}_7$ , on the other hand, remains hexagonal at all investigated temperatures [12] but reveals a long-range magnetic order below  $T_N = 160$  K (typically referred to as the  $\sqrt{3} \times \sqrt{3}$  structure),

at least partially, since a significant amount of diffuse scattering was still present between the magnetic Bragg peaks [13] at low temperatures. It was shown by simultaneous x-ray diffraction and absorption experiments that the oxygen intake and release at elevated temperatures is responsible for the resulting symmetry of the swedenborgite atomic lattice [14]. Naturally, the structural distortions in orthorhombic swedenborgites relieve the geometrical frustration and lead to long-range order with sharp, resolution-limited Bragg reflections in neutron diffraction experiments as reported for  $\text{YbBaCo}_4\text{O}_7$  [15],  $\text{CaBaCo}_4\text{O}_7$  [16,17],  $\text{CaBaFe}_4\text{O}_7$  [18–20], and  $\text{CaBaCo}_3\text{FeO}_7$  [21], where in some cases, the transition temperature is close to room temperature (RT). Additionally, the single-ion (magnetocrystalline) anisotropy effects may affect the symmetry and magnetism [19]. Some swedenborgite compounds [22] have attracted enormous interest due to their magnetoelectric properties under the application of an external magnetic field, which is directly linked to the highly interesting research topic of multiferroics [23,24]. In line with the Mermin-Wagner theorem [25], the triangular layer of magnetic ions between the kagome layers of the swedenborgite structure (Fig. 1) plays a decisive role in establishing long-range ordered magnetic structures, as it facilitates the magnetic coupling between the kagome layers, especially when magnetic ions with minor magnetocrystalline anisotropy are involved. The magnetic coupling is effectuated via superexchange pathways either within the kagome planes (TM2-O-TM2) or between the neighboring layers (TM1-O-TM2). In this paper, we present the magnetic properties of another magnetic swedenborgite with mixed TMs,  $\text{CaBaMn}_2\text{Fe}_2\text{O}_7$ , which remains in the hexagonal space group  $P6_3mc$  down to low temperatures. Magnetometry and specific

\*qureshi@ill.fr

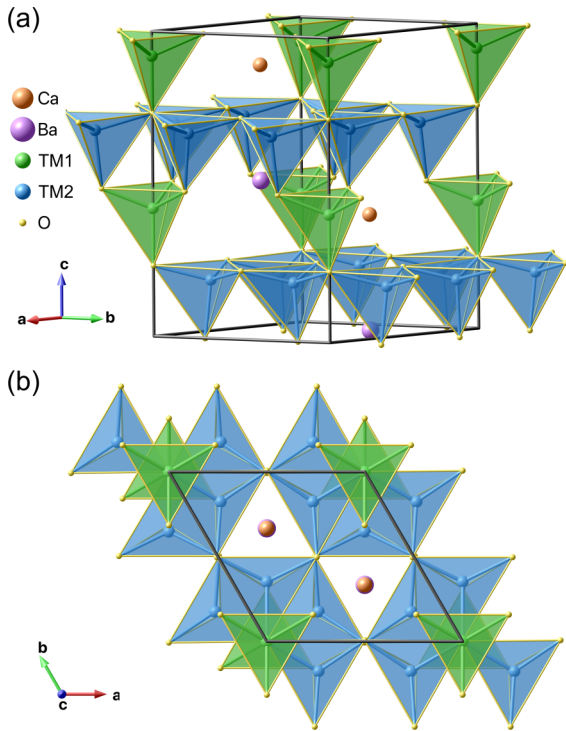


FIG. 1. (a) Visualization of the crystal structure of  $\text{CaBa(TM)}_4\text{O}_7$  consisting of triangular TM1 sites (green) and hexagonal TM2 sites (blue), where the latter form the kagome planes within the  $a$ - $b$  plane. (b) View along the  $c$  axis emphasizing the hexagonal symmetry and the location of the trigonal sites with respect to the kagome sites above and below.

heat measurements revealed a long-range antiferromagnetic ordering below  $T_N = 205.5$  K [26]. The powder neutron diffraction experiments presented here unambiguously reveal the magnetic structure below  $T_N$  which is backed up by Mössbauer spectroscopy measurements. The negligible amount of diffuse scattering in comparison with the strong Bragg peak intensities points toward the fact that  $\text{CaBaMn}_2\text{Fe}_2\text{O}_7$  is the only hexagonal swedenborgite with an almost fully ordered magnetic ground state.

## II. EXPERIMENTAL DETAILS

In this paper, powder samples were employed originating from the same batch that was used for the experiments reported in Ref. [26]. Powder neutron diffraction experiments were performed on the high-flux diffractometer D1B at the Institut Laue-Langevin (Grenoble, France) using a 350 mg sample within a sample holder made from vanadium, which has a negligible neutron coherent scattering length and therefore only contributes to the incoherent background. The instrument was equipped with a standard orange cryostat with a temperature range of  $\sim 1.5$ –300 K and a radial oscillating collimator to reduce parasitic scattering from the sample environment. A wavelength of 2.52 Å from the (002) reflection of the pyrolytic graphite monochromator was used. Long acquisition runs of 3 h were recorded at RT, 215, 190, and 1.5 K. The temperature dependence was investigated with short acquisition runs of 3 min and a controlled warming

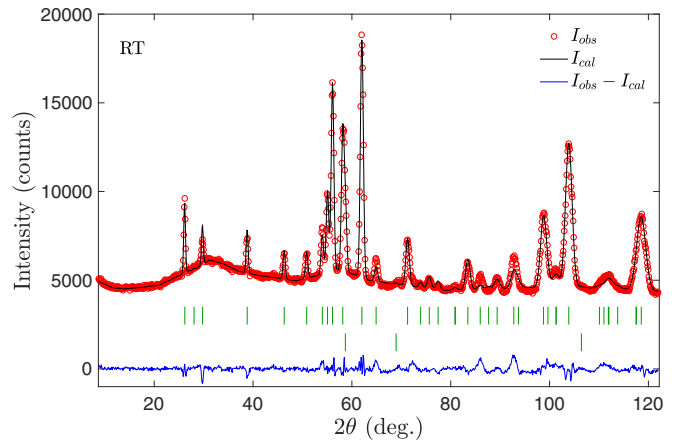


FIG. 2. Observed (red dots) and calculated (black solid line) diffraction patterns at room temperature (RT) and with the difference curve shown (in blue) at the bottom. The first row of green markers indicates the position of nuclear Bragg peaks of  $\text{CaBaMn}_2\text{Fe}_2\text{O}_7$  within the  $P6_3mc$  space group, whereas the second row denotes the peak positions of the impurity phase MnO (space group  $Fm\bar{3}m$ ,  $a = 4.4615$  Å).

rate of 0.4 K/min from 2 to 190 K, 0.1 K/min from 190 to 210 K, and again 0.4 K/min from 210 K to RT. All diffraction patterns were analyzed using the MAG2POL program [27].  $^{57}\text{Fe}$  Mössbauer spectra were collected at temperatures between 6 and 290 K using a standard WissEl spectrometer operated in the constant acceleration mode ( $^{57}\text{Co}/\text{Rh}$  source) and a Janis SHI 850-5 closed cycle refrigerator. About 45 mg of  $\text{CaBaMn}_2\text{Fe}_2\text{O}_7$  powder was mixed with BN and distributed in an acrylic glass sample container with an inner diameter of 13 mm. The data were evaluated with the MOSSWINN program [28] using the thin absorber approximation. The Mössbauer parameters, namely, the isomer shifts (ISs), quadrupole splittings (QSs), and hyperfine fields, were obtained by fitting the spectra to a superposition of doublets in the paramagnetic phase and six-line patterns in the magnetically ordered phase. Lorentzian line shapes with variable linewidths were assumed. All ISs are given relative to that of  $\alpha$ -iron.

## III. RESULTS

### A. Powder neutron diffraction

#### 1. Crystal structure

The analysis of the diffraction pattern recorded at RT confirmed the hexagonal crystal structure reported in Ref. [26] and the presence of an impurity phase MnO which was refined to 3.8(2) wt. %. Furthermore, due to the strikingly different neutron scattering lengths of Fe ( $b_{\text{Fe}} = 0.945 \times 10^{-12}$  cm) and Mn ( $b_{\text{Mn}} = -0.373 \times 10^{-12}$  cm) from their comparable number of electrons, it was possible to refine the occupation on both Wyckoff sites  $2a$  and  $6c$ . A reasonable fit (see Fig. 2) could only be achieved with a nonzero Mn occupation of  $O_{\text{Mn},2a} = 0.182(7)$  on the  $2a$  site, while a more homogeneous mixing is present on the  $6c$  site with  $O_{\text{Mn},6c} = 0.513(3)$ . Note that this result was inaccessible with x-ray diffraction employed in the original work [26]. The refined composition is therefore  $\text{CaBaMn}_{1.72}\text{Fe}_{2.28}\text{O}_{7+x}$ , confirming the expected

TABLE I. Structural parameters of  $\text{CaBaFe}_2\text{Mn}_2\text{O}_7$  within space group  $P6_3mc$  derived at different temperatures. Note that the origin was arbitrarily fixed by setting  $\text{Ba } z = 0$ . The refined lattice parameters are  $a = b = 6.418(1)$  Å and  $c = 10.389(2)$  Å at RT ( $R_F = 11.2$ ),  $a = b = 6.4137(2)$  Å and  $c = 10.3776(7)$  Å at 215 K ( $R_F = 10.9$ ),  $a = b = 6.4121(2)$  Å and  $c = 10.3769(6)$  Å at 190 K ( $R_F = 10.1$ ) as well as  $a = b = 6.4096(4)$  Å and  $c = 10.3657(7)$  Å at 2 K ( $R_F = 8.5$ ). The occupation factors of Fe and Mn as well as instrumental parameters were refined at RT and fixed for the refinements at lower temperatures.

Atoms	$T$ (K)	$x$	$y$	$z$	Occupation	
Ca ( $2b$ )	298	$\frac{1}{3}$	$\frac{2}{3}$	0.380(2)	1	
	215	$\frac{1}{3}$	$\frac{2}{3}$	0.378(2)		
	190	$\frac{1}{3}$	$\frac{2}{3}$	0.381(2)		
	1.5	$\frac{1}{3}$	$\frac{2}{3}$	0.388(3)		
	298	$\frac{1}{3}$	$\frac{2}{3}$	0.000		
Ba ( $2b$ )	215	$\frac{1}{3}$	$\frac{2}{3}$	0.000	1	
	190	$\frac{1}{3}$	$\frac{2}{3}$	0.000		
	1.5	$\frac{1}{3}$	$\frac{2}{3}$	0.000		
	298	0	0	0.418(2)		0.818(7)
	215	0	0	0.417(2)		
190	0	0	0.423(2)			
1.5	0	0	0.430(4)			
298	0	0	0.418(2)	0.182(7)		
215	0	0	0.417(2)			
190	0	0	0.423(2)			
1.5	0	0	0.430(4)			
298	0.352(1)	0.176(1)	0.179(2)		0.487(3)	
215	0.352(1)	0.176(1)	0.178(2)			
190	0.3482(9)	0.1741(9)	0.183(2)			
1.5	0.3468(7)	0.1734(7)	0.189(3)			
298	0.352(1)	0.176(1)	0.179(2)	0.513(3)		
215	0.352(1)	0.176(1)	0.178(2)			
190	0.3482(9)	0.1741(9)	0.183(2)			
1.5	0.3468(7)	0.1734(7)	0.189(3)			
298	0.0070(9)	0.5035(9)	0.223(2)		1	
215	0.0080(9)	0.5040(9)	0.224(2)			
190	0.010(1)	0.505(1)	0.227(2)			
1.5	0.012(1)	0.506(1)	0.230(3)			
298	0	0	0.230(2)	1		
215	0	0	0.232(2)			
190	0	0	0.236(2)			
1.5	0	0	0.242(3)			
298	0.1575(8)	0.8425(8)	0.487(2)		1	
215	0.1585(8)	0.8415(8)	0.487(2)			
190	0.1584(6)	0.8416(6)	0.491(2)			
1.5	0.1596(9)	0.8404(9)	0.490(3)			

surplus of Fe in the original work [26], also agreeing with the observation of a minor MnO impurity. The possible slight oxygen excess of  $x = 0.14$  (charge neutrality) may form octahedral defects as reported in Ref. [29] which, however, cannot be addressed due to the small extent and based on the present high-flux data. Due to the broad bump around  $2\theta = 30^\circ$  originating from strong magnetic diffuse scattering, the background was modeled using a linear interpolation between refinable points. The refined structural parameters at RT are listed in Table I. At lower temperatures, our data confirm that the system remains in the hexagonal space group  $P6_3mc$

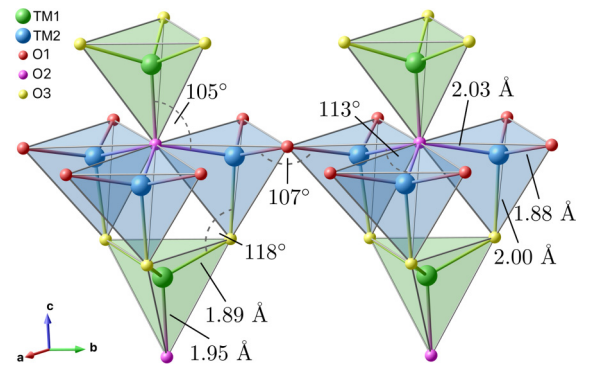


FIG. 3. Fraction of the swedenborgite structure focusing on two TM1-TM2-TM1 blocks connected via the O1 site within the kagome plane. Different bond lengths and angles are annotated in the figure. Within one block, the TM1-TM2 bond lengths are 3.16 and 3.35 Å, while that for TM2-TM2 is 3.39 Å. The distance between two TM2 atoms of different blocks is 3.03 Å.

with no significant change in the atomic parameters. Figure 3 visualizes the bond lengths and angles based on the refined structural parameters.

## 2. Magnetic structure

The magnetic properties were first investigated by focusing on the transition temperature between the paramagnetic and the long-range ordered state. Diffraction patterns were recorded as a function of temperature between 2 and 298 K, as shown in Fig. 4(a), and for a smaller temperature range in Fig. 4(b). The appearance of magnetic satellites was evident at scattering angles  $32.0^\circ$ ,  $14.9^\circ$ ,  $40.6^\circ$ , and  $43.1^\circ$  among others, from which the first was  $\sim 2.5\times$  stronger than the strongest nuclear reflection. The positions of these purely magnetic Bragg peaks can be indexed by a propagation vector  $\mathbf{q} = (\frac{1}{3} \frac{1}{3} 0)$ , i.e., the magnetic unit cell ( $3a, 3b, c$ ) is tripled along the  $a$  and  $b$  axes with respect to the nuclear one. The parasitic phase MnO itself reveals a magnetic phase transition at  $T \approx 120$  K which is manifest in the strong magnetic satellite reflection  $(\frac{1}{2} \frac{1}{2} \frac{1}{2})$  at  $2\theta = 28.5^\circ$  expressed in Miller indices corresponding to the conventional nuclear cell (i.e., with a magnetic unit cell doubled along all three axes). Figure 4(b) exhibits how the magnetic diffuse scattering around  $2\theta = 32^\circ$  transforms into a sharp resolution-limited Bragg reflection  $< \sim 205$  K, which corresponds very well with the reported Néel temperature [26] derived from specific heat and magnetization measurements on the same sample batch. With respect to the crystal structure, the magnetic ordering goes along with an inflection point in the temperature evolution of the lattice parameter  $c$ , ceasing to decrease with decreasing temperature [shown in Fig. 4(c)] which may be related to magnetoelastic coupling in this system. At  $\approx 175$  K,  $c$  is again decreasing when lowering the temperature, which will be discussed later. However, the low acquisition runs during the temperature variation do not permit any clear conclusions on eventual anomalies in the lattice constants due to the relatively large error bars. As the title compound has the same space group, crystal structure, and propagation vector as that of  $\text{CaBaCo}_2\text{Fe}_2\text{O}_7$ ,

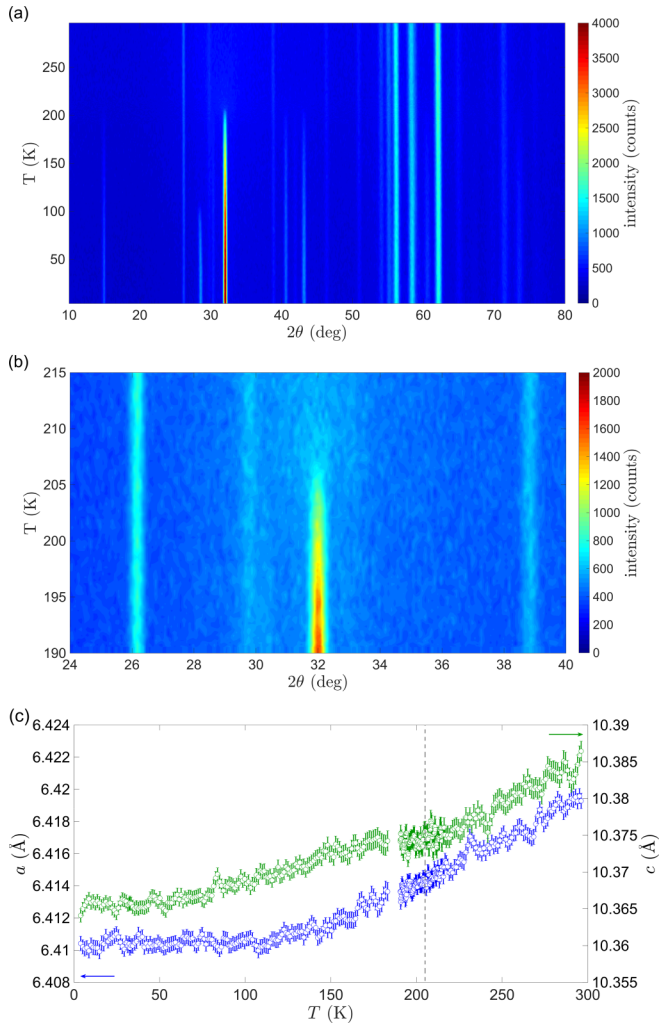


FIG. 4. (a) Thermodiffractogram taken upon controlled warming from 2 K to room temperature (RT). Magnetic satellites, not coinciding with predicted peak positions of the paramagnetic cell, can be observed below  $T \sim 205$  K and, e.g., at scattering angles  $14.9^\circ$ ,  $32.0^\circ$ ,  $40.6^\circ$ , and  $43.1^\circ$ . These purely magnetic intensities can be indexed with a propagation vector  $\mathbf{q} = (\frac{1}{3} \frac{1}{3} 0)$ . The onset of magnetic order of the parasitic phase MnO can be observed at  $T \approx 105$  K based on the  $(\frac{1}{2} \frac{1}{2} \frac{1}{2})$  reflection at  $2\theta = 28.5^\circ$ . (b) Same data as in (a) but focusing on the temperature region around  $T_N$  where the broad diffuse feature around  $2\theta = 32^\circ$  transforms to the strong and sharp  $(\frac{1}{3} \frac{1}{3} 2)$  reflection. (c) Refined lattice parameters  $a$  (blue circles, left axis) and  $c$  (green circles, right axis) as a function of temperature indicating an inflection point of the lattice parameter  $c$  at the magnetic phase transition (dashed line).

we also consider the same suggested magnetic space groups, i.e.,  $P6_3c'm'$ ,  $P6_3cm'$ ,  $P6_3c'm$ ,  $P6_3cm$ ,  $P31m'$ , and  $P31m$ . The four hexagonal magnetic space groups were not suited to explain the observed diffraction pattern at  $T = 1.5$  K which is due to the fact that, for hexagonal symmetry, the  $a$  and  $b$  components of the trigonal spins are forbidden, as already pointed out in Ref. [13]. The magnetic space groups  $P31m$  and  $P31m'$ , on the other hand, explain the observed magnetic intensities very well. The magnetic structures differ concerning the spin direction with respect to the trigonal axes, i.e.,  $\mu \parallel \langle 1\bar{1}0 \rangle$  in

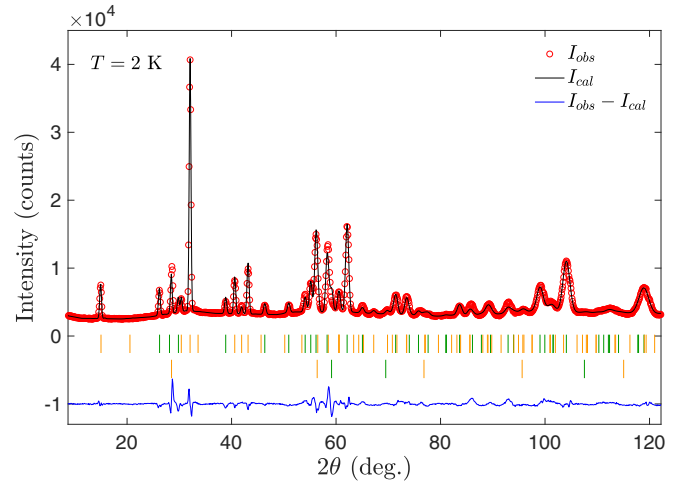


FIG. 5. Observed (red dots) and calculated (black solid line) diffraction patterns at  $T = 2$  K and with the difference curve shown (in blue) at the bottom. The first row of green (orange) markers indicates the position of nuclear (magnetic) Bragg peaks of  $\text{CaBaMn}_2\text{Fe}_2\text{O}_7$  within the  $P6_3mc$  space group, whereas the second row denotes the peak positions of the impurity phase MnO (space group  $Fm\bar{3}m$ ,  $a = 4.4615$  Å).

$P31m$  [Fig. 6(a)] and  $\mu \parallel \langle 100 \rangle$  in  $P31m'$  [Fig. 6(b)], and cannot be distinguished for a perfect, uncanted  $120^\circ$  block structure. Nevertheless, the spin canting patterns within the  $a$ - $b$  plane and along the  $c$  axis are different and would allow the real symmetry to be identified based on the presented neutron diffraction data. However, in both models, the deviation of the ordered moment from the main respective symmetry axes is insignificant, as suggested by the refined spin components, but especially by the absence of the  $(\frac{1}{3} \frac{1}{3} 1)$  reflection at  $2\theta = 20.6^\circ$  which is sensitive to both the in-plane and out-of-plane canting. Therefore, the observed magnetic scattering can be explained with essentially two free parameters corresponding to the magnetic moment size of the trigonal and kagome sites, which were refined to  $3.91(4)$  and  $3.82(2) \mu_B$  ( $R_F = 8.5$ ,  $R_{F,\text{mag}} = 15.3$ , whereas  $R_{F,\text{mag}} = 6.7$  for the well isolated magnetic peaks below  $2\theta = 45^\circ$ ). The observed and refined diffraction patterns are shown in Fig. 5.

The resulting magnetic structure is shown in Fig. 6 with respect to the trigonal magnetic unit cell which is  $\sqrt{3} \times$  longer along the  $a$  and  $b$  axes and rotated by  $90^\circ$ , as indicated by the conventional hexagonal unit cell. The magnetic moments arranged in triangular motifs within a kagome plane (emphasized by green bonds in Fig. 6) are antiferromagnetically coupled to their vertically displaced neighbor within the trigonal plane, which itself is again antiferromagnetically coupled to the next triangle of kagome spins. The collinear spin direction within such a cluster rotates by  $120^\circ$  for a translation along the  $a$  or the  $b$  axis of the conventional hexagonal cell characteristic of a cycloidal modulation. Note that the three closest kagome spins from three different clusters reveal a  $120^\circ$  configuration reminiscent of a geometrically frustrated antiferromagnetic coupling. The microscopic origin of this spin arrangement lies in the strong antiferromagnetic TM1-O-TM2 interactions between the trigonal and kagome planes (cf. Fig. 3)

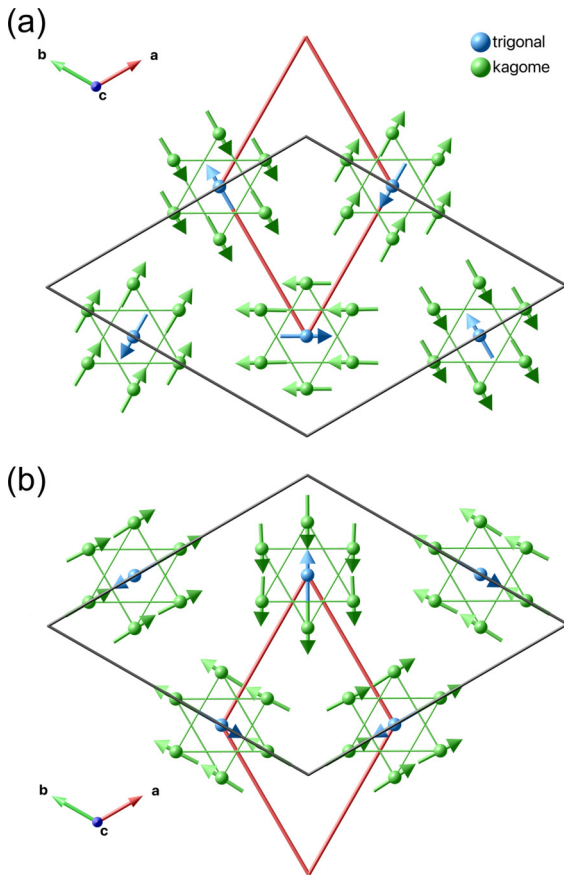


FIG. 6. Visualization of the magnetic structure of  $\text{CaBaMn}_2\text{Fe}_2\text{O}_7$  with respect to the trigonal magnetic unit cell (black lines) which is  $3\times$  bigger and rotated by  $90^\circ$  with respect to the conventional hexagonal unit cell (red lines). (a)  $P31m$  symmetry with the ordered magnetic moments along the  $[1\bar{1}0]$ ,  $[210]$ , and  $[120]$  directions and (b)  $P31m'$  symmetry with the main symmetry directions along  $[100]$ ,  $[110]$ , and  $[010]$ . In the absence of spin canting, the magnetic structures are indistinguishable in neutron diffraction experiments. The spins in the trigonal layer couple antiferromagnetically to the nearest kagome spins along the  $c$  axis, and the parallel alignment of the latter is emphasized by green bonds.

combined with the similarly strong but frustrated antiferromagnetic TM2-O-TM2 interactions within the kagome planes.

The analysis of the diffraction pattern recorded at  $T = 190$  K with equally long acquisition time yields the same type of magnetic structure, however, with different moment sizes for the different layers, i.e.,  $2.38(4)$  and  $2.00(2)\mu_B$  ( $R_F = 10.1$ ,  $R_{F,\text{mag}} = 20.7$ , whereas  $R_{F,\text{mag}} = 8.6$  for the well isolated magnetic peaks below  $2\theta = 45^\circ$ ) for the trigonal and kagome spins, respectively. Whether the second inflection point in the temperature dependence ( $T \approx 175$  K) of the lattice parameter  $c$  [cf. Fig. 4(c)] is related to the modified coupling between trigonal and kagome spins remains speculative and cannot be addressed based on the present data.

### 3. Magnetic diffuse scattering

The evolution of magnetic diffuse scattering between the sharp Bragg peaks was qualitatively analyzed by compar-

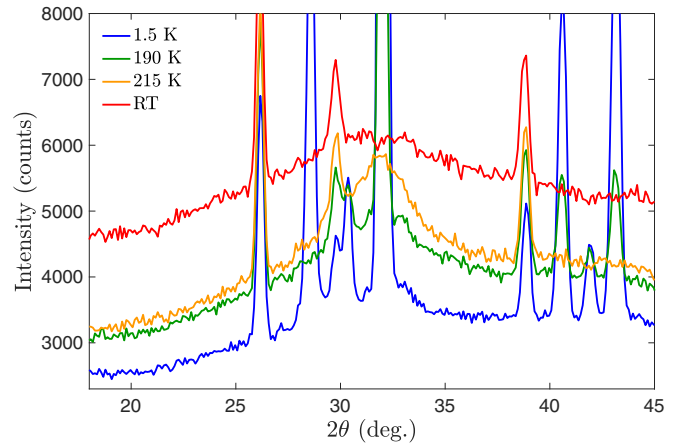


FIG. 7. Section of the recorded diffraction pattern focusing on the magnetic diffuse scattering around the  $(\frac{1}{3}, \frac{1}{3}, 2)$  reflection at  $2\theta = 32^\circ$ . While short-range correlations seem to be present at room temperature, i.e., far above  $T_N$ , a minimal amount of disorder appears to persist down to the lowest measured temperature of 1.5 K. Note that the peak intensity of the strong magnetic  $(\frac{1}{3}, \frac{1}{3}, 2)$  reflection at  $2\theta = 32^\circ$  is  $>40\,000$  counts.

ing the long acquisition runs at four different temperatures. Figure 7 shows a section of the measured diffraction pattern centered at the position of the strongest magnetic reflection  $(\frac{1}{3}, \frac{1}{3}, 2)$  at  $2\theta = 32^\circ$ . At RT, a very broad feature can be observed, suggesting short-ranged correlations far above the magnetic transition temperature of 205 K. At 215 K, the diffuse scattering is much more localized before a coexistence with the resolution-limited Bragg reflection is present at 190 K. At the lowest investigated temperature,  $T = 1.5$  K, a very small amount of diffuse scattering intensity is still visible at the tail of the Bragg reflection, indicating that the magnetic moments are not completely ordered. By integrating the peak intensities of both Bragg and diffuse contributions, an approximate ratio can be determined, where the ordered component is  $\sim 20\times$  stronger than the disordered one, which is strikingly different from the  $\text{CaBaCo}_2\text{Fe}_2\text{O}_7$  compound in which strong magnetic diffuse scattering between the Bragg peaks was observed down to 4 K in combination with significantly reduced ordered magnetic moment amplitudes [13]. Note that, in this paper, the weak diffuse scattering was not visible in the short acquisition runs.

### B. Mössbauer spectroscopy

In Fig. 8, the evolution of the Mössbauer spectra with temperature is shown. At temperatures above 200 K, the compound is in the paramagnetic phase, and the spectra consist of an asymmetric strongly broadened quadrupole doublet structure. For  $T \leq 200$  K, the spectra reveal magnetic hyperfine splitting for all Fe sites, which is consistent with the reported long-range magnetic ordering with  $T_N \sim 206$  K [26]. The broadening and asymmetry of the spectra in the paramagnetic phase (Fig. 9) indicate that the spectrum is composed of several subspectra with somewhat different hyperfine interaction parameters. The crystal structure of the swedenborgite-type  $\text{CaBaMn}_2\text{Fe}_2\text{O}_7$  comprises two different

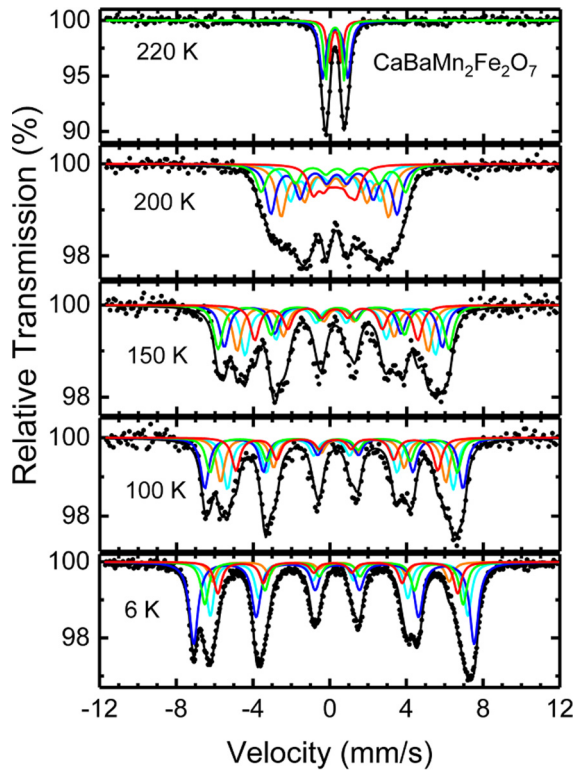


FIG. 8. Temperature dependence of the Mössbauer spectra of  $\text{CaBaMn}_2\text{Fe}_2\text{O}_7$ . Dots correspond to the experimental data, black solid lines to the calculated spectra, and the colored lines to the components which were used for modeling the spectra to extract the temperature dependence of the mean hyperfine field as a measure of the order parameter.

lattice sites for the TM ions, namely, the trigonal ( $\text{Mn1,Fe1}$ ) site on Wyckoff positions  $2a$  and the kagome ( $\text{Mn2,Fe2}$ ) sites on Wyckoff positions  $6c$ . However, owing to the presence of two different TM ions and the resulting atomic disorder, the local environment of the Fe ions varies, and the observed spectra depend on the distribution of the ions between the two sites in the crystal structure and on the varying number of nearest neighbor Mn ions around a given Fe ion. Here, we have fitted the spectra above  $T_N$  to a superposition of three quadrupole doublets. This model results in similar ISs ( $\sim 0.21$  mm/s at RT) but different QSs (0.72, 1.01, and 1.32 mm/s) for the three doublets. This reflects the variation in the local environment of the various Fe sites which leads to different electric field gradients (EFGs) and thus different interactions with the nuclear quadrupole moment of the excited  $I = \frac{3}{2}$  state of the  $^{57}\text{Fe}$  nucleus. The quite small IS as well as the nearly temperature-independent QS values confirm that all Fe sites correspond to  $\text{Fe}^{3+}$  ions. This clue is corroborated by the analysis of the Mössbauer spectrum at 6 K (Fig. 9). The complex shape of the spectrum was modeled by assuming a superposition of five six-line patterns arising from the nuclear Zeeman effect and differing in their QS parameters  $QS'$  and their magnetic hyperfine fields  $B_{\text{hf}}$ . Note that  $QS'$  is determined by the EFGs as well as by the orientation angles between the EFGs and  $B_{\text{hf}}$ . Remarkably, the outer line in the low-velocity region of the spectrum is quite well resolved.

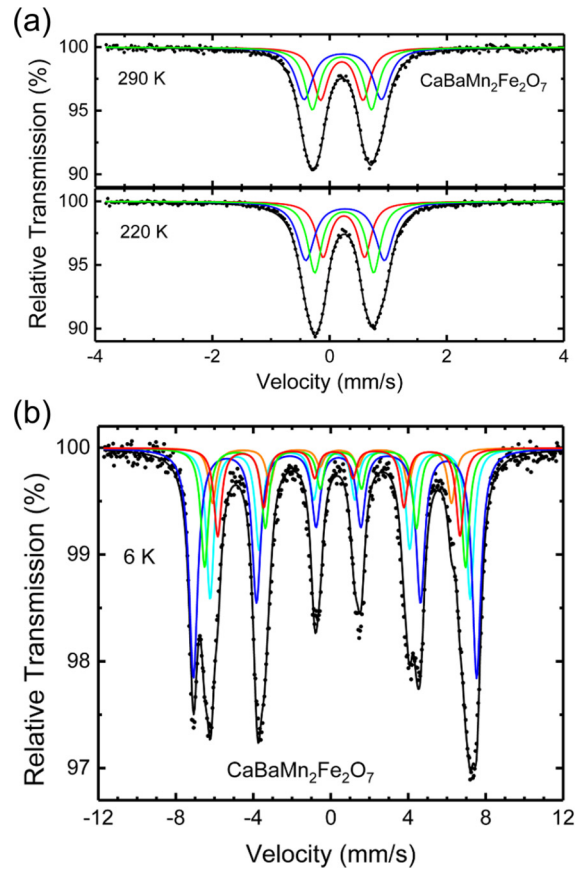


FIG. 9. (a) Mössbauer spectra of  $\text{CaBaMn}_2\text{Fe}_2\text{O}_7$  at 220 and 290 K in the paramagnetic phase. (b) Mössbauer spectrum of  $\text{CaBaMn}_2\text{Fe}_2\text{O}_7$  at 6 K. Dots correspond to the experimental data, black solid lines to the calculated spectrum, and the colored lines to the components used for modeling the spectra. The different components reflect the variation in the local environment of the Fe ions owing to Fe/Mn disorder. As discussed in the text, the outer (blue) six-line pattern in (b) is tentatively assigned to Fe1 sites.

Thus, we have firstly used two IS values, one for the sextet involving the resolved component and one for the other components of which the ISs and linewidths were assumed to be equal. Using this model, the gross features of the spectrum could be reproduced. A minor increase in the quality of the fits was obtained by allowing for different IS values for all components, which could indicate a certain variation of IS with varying local environment of the  $\text{Fe}^{3+}$  ions. However, the weighted average IS value of these components (0.32 mm/s) is like that of the first component (0.31 mm/s) and in agreement with tetrahedral  $\text{FeO}_4$  coordination. This result is in contrast to the related system  $\text{YBaCo}_3\text{FeO}_7$  containing  $\text{Co}^{2+}$ ,  $\text{Co}^{3+}$ , and  $\text{Fe}^{3+}$  ions where the ISs of  $\text{Fe}^{3+}$  on the  $2a$  and  $6c$  sites were reported to be considerably different ( $\sim 0.3$  and  $\sim 0.45$  mm/s at 4 K, respectively) [30]. The IS value of 0.31 mm/s and  $B_{\text{hf}}$  value of 45 T of the outer component in the spectrum of  $\text{CaBaMn}_2\text{Fe}_2\text{O}_7$  [Fig. 9(b)] are quite close to those for the Fe1 site in  $\text{YBaCo}_3\text{FeO}_7$  ( $\sim 0.30$  mm/s and  $\sim 43$  T) [30], and it is tempting to assign this subspectrum to the trigonal Fe1 ( $2c$ ) sites. This assignment is supported by the quite good agreement between the area fraction of 39% of the

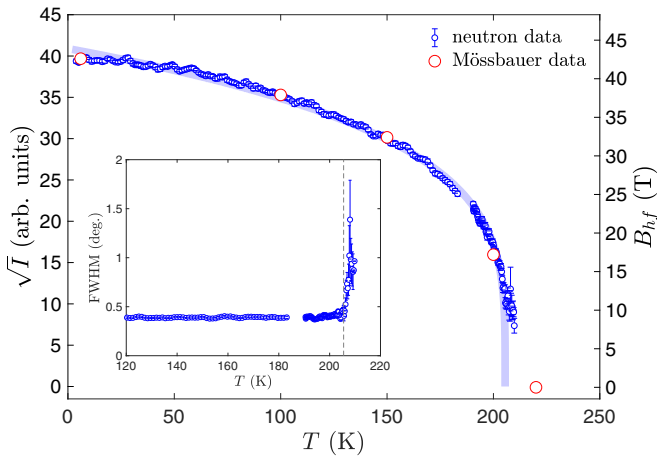


FIG. 10. Mean magnetic hyperfine field  $B_{\text{hf}}$  (red dots) extracted from the Mössbauer spectra as a function of temperature compared with the square root of the integrated intensities of the magnetic  $(\frac{1}{3} \frac{1}{3} 2)$  reflection (blue dots) observed in the powder neutron diffraction patterns. Both are a measure for the order parameter in the system to which a power law  $\propto (1 - T/T_N)^\beta$  has been fitted as a guide to the eye (blue line, see main text). The transition temperature has been fixed to 205.5 K as revealed by the departure of the full width at half maximum (FWHM) from that of the resolution-limited diffraction peaks (inset) which is in perfect agreement with Ref. [26].

outer sextet and the fraction of 36% Fe1 sites with respect to the total Fe content calculated from the occupancies according to the neutron data (Table I). Then the other subspectra are possibly related to the 6c positions where disorder between smaller  $\text{Fe}^{3+}$  and larger  $\text{Mn}^{2+}$  will lead to a variation in the local environment and exchange interactions of the Fe ions and thus to components with somewhat different  $B_{\text{hf}}$  and QS' parameters. Furthermore, additional oxygen sites may contribute to local atomic disorder which is expected to modify the local exchange interactions. In contrast to  $\text{YBaCo}_3\text{FeO}_7$ , the  $B_{\text{hf}}$  values of the other subspectra are  $< 45$  T, while the kagome Fe2 sites in  $\text{YBaCo}_3\text{FeO}_7$  revealed increased average  $B_{\text{hf}}$  values (53 T) [30]. In the present system, the  $B_{\text{hf}}$  values of the other components vary between 38 and 41 T. The distribution in  $B_{\text{hf}}$  could arise from a certain variation of the magnetic moment at the different Fe sites and from dipolar contributions to  $B_{\text{hf}}$  owing to the variation in local environment. The temperature dependence of the individual magnetic hyperfine field components has little informative value due to the fact that they cannot be unambiguously attributed to well-defined sites in the phenomenological fits. However, the weighted mean  $B_{\text{hf}}$  value is a measure for the order parameter of the system and is depicted in Fig. 10 together with the square root of the integrated intensity of the strongest magnetic reflection in the neutron diffraction patterns. Very good agreement between the two techniques is apparent and the temperature evolution follows a power law  $\propto (1 - T/T_N)^\beta$ . Due to the large amount of diffuse scattering above  $T_N$ , the Gaussian fits to the peak profile do not correctly represent the transition into the paramagnetic phase, for which it is not possible to extract a reliable critical exponent, as the power law fit is very sensitive to the critical region and  $T_N$  itself. Therefore, we have constrained  $T_N$  in the power law

fit (serving as a guide to the eye only) of the neutron data to the value at which a clear departure from the resolution-limited full width at half maximum (FWHM) is observed (inset of Fig. 10), which coincides with the reported value of 205.5 K.

#### IV. SUMMARY AND CONCLUSIONS

We have presented the magnetic properties of a mixed TM swedenborgite,  $\text{CaBaMn}_2\text{Fe}_2\text{O}_7$ , by combining neutron diffraction and  $^{57}\text{Fe}$  Mössbauer techniques on polycrystalline samples. Both experiments reveal a transition into a magnetically ordered state at  $T_N = 205$  K which agrees very well with the previous report [26] based on specific heat and magnetization measurements on the same sample batch. The square root of the integrated magnetic Bragg intensities (neutron scattering) and the mean magnetic hyperfine fields (Mössbauer) are a measure of the order parameter and follow the same temperature evolution, which can be fitted to a power law. However, the difficulty in determining the exact Bragg peak intensities very close to  $T_N$  due to the presence of strong diffuse scattering does not allow us to extract a reliable critical exponent. Further powder neutron diffraction data with long acquisition times or even complementary single-crystal experiments are necessary to comment on the spin dimensionality of this system, which, however, does not question the essential results concerning the magnetic structure presented here. Our neutron data unambiguously reveal the classical  $\sqrt{3} \times \sqrt{3}$  magnetic structure on a hexagonal lattice with propagation vector  $\mathbf{q} = (\frac{1}{3} \frac{1}{3} 0)$  with antiferromagnetic coupling between neighboring kagome and trigonal spins and a  $120^\circ$  rotation of spin direction for a translation along either the  $a$  or  $b$  axis. The sense of this rotation is determined by the magnetic space group being either  $P31m$  or  $P31m'$ , which in the absence of spin canting away from the high-symmetry directions  $(1\bar{1}0)$  in  $P31m$  and  $(100)$  in  $P31m'$  cannot be distinguished in an unpolarized neutron experiment because both spin configurations yield the same magnetic intensities. However, due to the inherently opposite chirality of the two possible magnetic structures, a spherical neutron polarimetry experiment can tell the difference by investigating the created/annihilated neutron beam polarization along the scattering vector after the scattering process, if an enantiopure single crystal (or at least a sample with a significant twin imbalance) can be synthesized. To unambiguously relate the magnetic chirality to the structural chirality, the latter needs to be determined by analyzing the Schwinger scattering of adequate reflections (see, e.g., Refs. [31,32]). We have identified several reasonably strong  $(hkl)$  reflections revealing a flipping ratio asymmetry of  $|R - 1| > 0.04$  which would be experimentally feasible. A magnetic structure very similar to the one presented here was reported in the likewise hexagonal compound  $\text{CaBaCo}_2\text{Fe}_2\text{O}_7$ . It must be noted that, despite the use of a single crystal and additional XYZ-polarization analysis, the magnetic space group could not be determined unambiguously although spin canting was present. However, in contrast to our study, significantly reduced magnetic moment amplitudes ( $2.73 \mu_B$  for the trigonal and  $2.19 \mu_B$  for the kagome site, respectively [13]) were observed due to the presence of significant short-range order as manifested by considerably

strong magnetic diffuse scattering between the Bragg peaks down to low temperatures. Here, for  $\text{CaBaMn}_2\text{Fe}_2\text{O}_7$ , a close inspection of the residual diffuse scattering at the tails of the strongest magnetic Bragg reflection suggests that the system is almost fully ordered, which is furthermore supported by the equally sized amplitudes of kagome and trigonal spins of almost  $4\mu_B$  in comparison to the theoretical  $5\mu_B$  for a mixture of  $\text{Fe}^{3+}$  and  $\text{Mn}^{2+}$   $S = \frac{5}{2}$  spins. Full magnetic order is also supported by the uniform evolution of the magnetic hyperfine pattern in the Mössbauer spectra, while magnetic disorder effects typically lead to paramagnetic signals even below  $T_N$  [33]. With respect to the expected charge states, the Mössbauer spectra do not show any signals pointing toward the presence of  $\text{Fe}^{2+}$ , which should have clearly different hyperfine parameters. Additionally, due to the constrained O content of the sample from evacuated ampoule synthesis conditions, the presence of  $\text{Mn}^{3+}$  in the sample is unlikely, suggesting the likelihood of a uniform  $S = \frac{5}{2}$  magnetic sublattice. The relatively high ordering temperature combined with a hexagonal crystal structure at all investigated temperatures and a negligible magnetic disorder attributes  $\text{CaBaMn}_2\text{Fe}_2\text{O}_7$  a special role among the magnetic swedenborgites, especially since all involved spins are without single-ion anisotropy (high-spin  $d^5$ ). This is a perfect example of how sensitive the magnetic lattices in the swedenborgites are to minor structural and compositional changes. The title compound exhibits a long-range spin-ordered ground state, while  $\text{YBaCo}_3\text{FeO}_7$  possesses a unique magnetic ground state with partial spin order [11]. By further changing the elemental composition but conserving the hexagonal (or trigonal) swedenborgite lattice, the magnetic ground state can be affected; the parent compound  $\text{YBaCo}_4\text{O}_7$  [9] is reported with both long-range magnetic order [34–36] and with short-range ordering [9,37]. The reason for this inconsistency is probably the exact

oxygen content of the individual samples. By introducing Ca at the Y site, thus changing also the average oxidation state of Co, diffuse neutron scattering was reported for partial replacement [38,39], and a structural transition with long-range magnetic ordering was observed for the composition  $\text{CaBaCo}_4\text{O}_7$  [40]. When replacing Co in  $\text{YBaCo}_4\text{O}_7$ , a manifold of magnetic ground states has been reported: a spin-liquid in  $\text{YBaCo}_3\text{FeO}_7$  [11], a mixture of long- and short-range ordering in  $\text{CaBaCo}_2\text{Fe}_2\text{O}_7$  [13], and further. As the swedenborgites are reported with various oxygen compositions, from stoichiometric 7.0 up to  $\sim 8.5$  [29,41], the oxidation states of the magnetic ions can be further controlled, with consequences for the magnetic properties (see, for example, Ref. [42]). The surplus of oxygen also accounts for lattice distortions, i.e., the hexagonal (trigonal) symmetry is lowered to orthorhombic, partly relieving the magnetic frustration within the kagome lattice. For the title compound, a synthesis in closed ampoules was used to restrict the oxygen composition to be nearly stoichiometric ( $\sim 7.0$ ), which not only seems to agree with the uniform  $3d^5$  spin lattice but also with the relatively high (hexagonal) lattice symmetry. Hence, the effects of structural and electronic alterations on the magnetic lattices of the swedenborgites offer challenges in fundamental magnetism. However, the combination of neutron scattering (global probe) and Mössbauer spectroscopy (local probe) is the key to understanding the challenging, magnetically frustrated lattice.

#### ACKNOWLEDGMENTS

We acknowledge the beam time [43] on the D1B instrument at the Institut Laue-Langevin. The research in Dresden was partially supported by the Deutsche Forschungsgemeinschaft through SFB 1143 (Project-Id 247310070).

- 
- [1] M. R. Norman, *Rev. Mod. Phys.* **88**, 041002 (2016).  
 [2] P. Mendels and F. Bert, *C. R. Phys.* **17**, 455 (2016).  
 [3] M. J. Harris and M. P. Zinkin, *Mod. Phys. Lett. B* **10**, 417 (1996).  
 [4] J. G. Rau and M. J. P. Gingras, *Annu. Rev. Condens. Matter Phys.* **10**, 357 (2019).  
 [5] A. P. Ramirez, *Annu. Rev. Mater. Sci.* **24**, 453 (1994).  
 [6] R. Moessner and A. P. Ramirez, *Phys. Today* **59**, 24 (2006).  
 [7] G. Aminoff and G. K. Almström, *Z. Kristallogr. Crst. Mater.* **60**, 262 (1924).  
 [8] G. Aminoff and R. Blix, *Kungl. Svenska Vetenskapskad. Handl.* **11**, 3 (1933).  
 [9] M. Valldor and M. Andersson, *Solid State Sci.* **4**, 923 (2002).  
 [10] M. Valldor, *J. Phys.: Condens. Matter* **16**, 9209 (2004).  
 [11] W. Schweika, M. Valldor, J. D. Reim, and U. K. Rößler, *Phys. Rev. X* **12**, 021029 (2022).  
 [12] J. D. Reim, E. Rosén, W. Schweika, M. Neven, N. R. Leo, D. Meiser, M. Fiebig, M. Schmidt, C.-Y. Kuo, T.-W. Pi *et al.*, *J. Appl. Crystallogr.* **47**, 2038 (2014).  
 [13] J. D. Reim, E. Rosén, O. Zaharko, M. Mostovoy, J. Robert, M. Valldor, and W. Schweika, *Phys. Rev. B* **97**, 144402 (2018).  
 [14] M. Valkeapää, M. Karppinen, T. Motohashi, R.-S. Liu, L.-M. Chen, and H. Yamauchi, *Chem. Lett.* **36**, 1368 (2007).  
 [15] A. Huq, J. F. Mitchell, H. Zheng, L. C. Chapon, P. G. Radaelli, K. S. Knight, and P. W. Stephens, *J. Solid State Chem.* **179**, 1136 (2006).  
 [16] V. Caignaert, A. Maignan, K. Singh, C. Simon, V. Pralong, B. Raveau, J. F. Mitchell, H. Zheng, A. Huq, and L. C. Chapon, *Phys. Rev. B* **88**, 174403 (2013).  
 [17] R. S. Fishman, S. Bordács, V. Kocsis, I. Kézsmárki, J. Viikro, U. Nagel, T. Rööm, A. Puri, U. Zeitler, Y. Tokunaga *et al.*, *Phys. Rev. B* **95**, 024423 (2017).  
 [18] B. Raveau, V. Caignaert, V. Pralong, D. Pelloquin, and A. Maignan, *Chem. Mater.* **20**, 6295 (2008).  
 [19] N. Hollmann, M. Valldor, H. Wu, Z. Hu, N. Qureshi, T. Willers, Y.-Y. Chin, J. C. Cezar, A. Tanaka, N. B. Brookes, and L. H. Tjeng, *Phys. Rev. B* **83**, 180405(R) (2011).  
 [20] N. Qureshi, B. Ouladdiaf, A. Senyshyn, V. Caignaert, and M. Valldor, *SciPost Phys. Core* **5**, 007 (2022).  
 [21] N. Qureshi, M. T. Fernández Díaz, L. C. Chapon, A. Senyshyn, W. Schweika, and M. Valldor, *Phys. Rev. B* **97**, 064404 (2018).



- [22] V. Kocsis, Y. Tokunaga, S. Bordács, M. Kriener, A. Puri, U. Zeitler, Y. Taguchi, Y. Tokura, and I. Kézsmárki, *Phys. Rev. B* **93**, 014444 (2016).
- [23] S.-W. Cheong and M. Mostovoy, *Nat. Mater.* **6**, 13 (2007).
- [24] M. Fiebig, T. Lottermoser, D. Meier, and M. Trassin, *Nat. Rev. Mater.* **1**, 16046 (2016).
- [25] N. D. Mermin and H. Wagner, *Phys. Rev. Lett.* **17**, 1133 (1966).
- [26] M. Valldor, R. Yadav, L. Hozoi, J. van den Brink, A. Maljuk, J. Werner, F. Scaravaggi, A. U. B. Wolter, and B. Büchner, *Z. Anorg. Allg. Chemie* **643**, 1543 (2017).
- [27] N. Qureshi, *J. Appl. Crystallogr.* **52**, 175 (2019).
- [28] Z. Klencsár, E. Kuzmann, and A. Vértes, *J. Radioanal. Nucl. Chem.* **210**, 105 (1996).
- [29] O. Chmaissem, H. Zheng, H. Huq, P. W. Stephens, and J. F. Mitchell, *J. Solid State Chem.* **181**, 664 (2008).
- [30] M. Valldor, R. P. Hermann, J. Wuttke, M. Zamponi, and W. Schweika, *Phys. Rev. B* **84**, 224426 (2011).
- [31] N. Qureshi, A. Bombardi, S. Picozzi, P. Barone, E. Lelièvre-Berna, X. Xu, C. Stock, D. F. McMorrow, A. Hearmon, F. Fabrizi *et al.*, *Phys. Rev. B* **102**, 054417 (2020).
- [32] E. Chan, J. Pásztorová, R. D. Johnson, M. Songvilay, R. A. Downie, J. W. G. Bos, O. Fabelo, C. Ritter, K. Beauvois, C. Niedermayer *et al.*, *Phys. Rev. B* **106**, 064403 (2022).
- [33] K. Naveen, T. Rom, S. S. Islam, M. Reehuis, P. Adler, C. Felser, A. Hoser, R. C. Nath, A. K. Yadav, S. N. Iha *et al.*, *Phys. Chem. Chem. Phys.* **23**, 21769 (2021).
- [34] M. Soda, Y. Yasui, T. Moyoshi, M. Sato, N. Igawa, and K. Kakurai, *J. Phys. Soc. Jpn.* **75**, 054707 (2006).
- [35] L. C. Chapon, P. G. Radaelli, H. Zheng, and J. F. Mitchell, *Phys. Rev. B* **74**, 172401 (2006).
- [36] D. D. Khalyavin, P. Manuel, B. Ouladdiaf, A. Huq, P. W. Stephens, H. Zheng, J. F. Mitchell, and L. C. Chapon, *Phys. Rev. B* **83**, 094412 (2011).
- [37] A. K. Bera, S. M. Yusuf, and S. Banerjee, *Solid State Sci.* **16**, 57 (2013).
- [38] M. Valldor, *Solid State Sci.* **8**, 1272 (2006).
- [39] S. Gao, V. Kocsis, M. Soda, F. Ye, Y. Liu, A. F. May, Y. Taguchi, Y. Tokura, T. H. Arima, W. Schweika *et al.*, *Phys. Rev. B* **104**, L140408 (2021).
- [40] V. Caignaert, V. Pralong, V. Hardy, C. Ritter, and B. Raveau, *Phys. Rev. B* **81**, 094417 (2010).
- [41] Y. Jia, H. Jiang, M. Valkepää, R. Dai, H. Yamauchi, M. Karppinen, and E. I. Kauppinen, *Solid State Ion.* **204–205**, 7 (2011).
- [42] S. Avcı, O. Chmaissem, H. Zheng, A. Huq, P. Manuel, and J. F. Mitchell, *Chem. Mater.* **25**, 4188 (2013).
- [43] R. Morrow and I. Puente-Orench, Magnetic Structure of Swedenborgite  $\text{CaBaMn}_2\text{Fe}_2\text{O}_7$ , Institut Laue-Langevin (ILL) (2019), doi:10.5291/ILL-DATA.EASY-468.